




# Macro-micron-nano-featured surface topography of Ti-6Al-4V alloy for biomedical applications

Da-Peng Zhao\* , Jin-Cheng Tang, He-Min Nie, Yuan Zhang, Yu-Kai Chen, Xu Zhang, Hui-Xing Li, Ming Yan

Received: 26 June 2018 / Revised: 9 August 2018 / Accepted: 22 August 2018 / Published online: 9 November 2018  
© The Nonferrous Metals Society of China and Springer-Verlag GmbH Germany, part of Springer Nature 2018

**Abstract** One of the critical issues in the development of novel metallic biomaterials is the design and fabrication of metallic scaffolds and implants with hierarchical structures mimicking human bones. In this work, selective laser melting (SLM) and electrochemical anodization were applied to fabricate dense Ti-6Al-4V components with macro-micron-nanoscale hierarchical surfaces. Scanning electron microscopy (SEM), 3D laser scanning microscopy (3D LSM), contact angle video system, fluorescence microscopy and spectrophotometer were used to investigate the properties of the samples. The results reveal that the SLMed post-anodization (SLM-TNT) exhibits enhanced or at least comparable wettability, protein adsorption and biological response of mesenchymal stem cells (MSCs) in comparison with the three reference configurations, i.e., the polished Ti-6Al-4V (PO-Ti64), the SLMed Ti-6Al-4V (SLM-Ti64) and the polished Ti-6Al-4V post-anodization (PO-TNT). The improved cytocompatibility of the samples after SLM and anodization should be mainly attributed to the nanoscale tubular features, while the macro-micron-scale structures only lead to slight preference for cell attachment.

**Keywords** Selective laser melting; Electrochemical anodization; Hierarchical surface; Cell adhesion; Cell proliferation

D.-P. Zhao\*, J.-C. Tang, H.-M. Nie, Y. Zhang, Y.-K. Chen  
College of Biology, Hunan University, Changsha 410082, China  
e-mail: dpzhao@hnu.edu.cn

X. Zhang, H.-X. Li, M. Yan  
Shenzhen Key Laboratory for Additive Manufacturing of High-Performance Materials, Department of Materials Science and Engineering, Southern University of Science and Technology, Shenzhen 518055, China

## 1 Introduction

Among numerous titanium (Ti) alloys, Ti-6Al-4V is still the most widely used one for biomedical applications, due to its superb corrosion resistance, high strength-to-weight ratio and good biocompatibility [1–4]. However, the fabrication of Ti-based implants is strongly limited by the costly and multi-step processing of conventional techniques [5, 6]. The additive manufacturing (AM) technologies, such as selective laser melting (SLM) and electron beam melting (EBM), offer an effective layer-by-layer approach to accurately fabricate customized implant components with nearly any geometry [7]. Many porous Ti-6Al-4V implants have been designed and fabricated to mimic spongy bones with trabeculae. Porous Ti-6Al-4V implants with 250- $\mu\text{m}$ -sized pores, produced via SLM process, have supported vessel ingrowth and bone formation [8]. EBM was applied for the fabrication of rationally designed porous Ti-6Al-4V biomaterials with high strength, low modulus and desirable deformation behavior [9]. The low fatigue strength of porous Ti-6Al-4V components produced via AM limits their applications as high load-bearing implants [10], so dense AM components are attracting increasing attentions. For example, Xu et al. [11] obtained Ti-6Al-4V biomaterials with superior strength and ductility by controlling  $\alpha'$  martensite decomposition during SLM process.

AM can obtain metallic surface features at hundreds of, or at best, tens of micron-scales. The resolution of AMed metallic products is limited by the minimum line width of powder fusing methods (usually tens of microns) [12]. Therefore, in order to improve the osseointegration of AM-processed Ti-6Al-4V implants, surface features at sub-micron-scale or below are usually introduced via various surface modification techniques [13]. Among these

techniques, electrochemical anodization provides a cost-efficient way to fabricate highly regular and controllable self-assembled titanium oxide ( $\text{TiO}_2$ ) nanotube (TNT) arrays on Ti-based biomaterials [14]. Electrochemical anodization is usually applied to obtain nano-features on AMed Ti-6Al-4V components [15], and the TNT arrays on AMed Ti-6Al-4V mesh structures have significantly improved the expression level of proteins and promoted bone formation [16]. It was reported that TNTs with a diameter of 70 nm on Ti-6Al-4V substrates stimulate the endothelial viability, adhesion and proliferation [17]. So far, most of these studies focused on the anodization on AM-processed porous Ti-6Al-4V implants as trabecular bone substitution, instead of dense Ti-6Al-4V components for high load-bearing applications [18]. Therefore, it is warranted to evaluate the surface properties and cell response of anodized AM-processed solid Ti-6Al-4V alloy. Mesenchymal stem cells (MSCs) are non-haematopoietic stromal stem cells and are capable of self-replication and contributing to the regeneration of bone [19], so they were chosen as model cells for the cytocompatibility assessments in the present work.

The purpose of this study is to produce solid Ti-6Al-4V components with hierarchical surface features by using SLM and electrochemical anodization, and to investigate the influence of the surface features at different scales on the surface properties and cell responses.

## 2 Experimental

### 2.1 Sample preparation

Raw Ti-6Al-4V powders were commercially purchased from EOS, Germany. The powders show good sphericity and flowability (Fig. 1a) with average powder size of  $\sim 35 \mu\text{m}$  (Fig. 1b). SLM (SLM solutions 125 HL) was used

to prepare Ti-6Al-4V samples ( $10 \text{ mm} \times 10 \text{ mm} \times 2.5 \text{ mm}$ ) by using laser power of 150 W, scanning speed of  $450 \text{ mm}\cdot\text{s}^{-1}$ , layer thickness of 0.03 mm and hatch distance of 0.45 mm. These SLMed samples show relative density ranging from 98% to 99%. Selected SLMed samples were used as substrates for electrochemical anodization. The samples were ultrasonically cleaned and then anodized for 90 min in a two-electrode electrochemical cell at a constant voltage of 20 V using a direct current (DC) power supply. During anodization, the electrolyte containing 0.5 wt%  $\text{NH}_4\text{F}$  was continuously agitated by a magnetic stirrer. After rinsed and dried, the anodized samples were annealed at  $450 \text{ }^\circ\text{C}$  for 2 h, in order to increase biocompatible anatase phase instead of amorphous  $\text{TiO}_2$ . As reference samples, Ti-6Al-4V extra low interstitial (ELI) disks (supplied by BaoTi Group, Co., Ltd., China) were wire-electrode cut into the same size as SLMed samples, followed by mechanical polishing with 50-nm  $\text{SiO}_2$  polishing agent and ultrasonic rinsing in deionized water. Selected Ti-6Al-4V ELI disks were then anodized following the same above-mentioned anodization process. The polished reference samples, the SLMed samples, the polishing-anodization-processed samples and the SLM-anodization-processed samples are termed to as PO-Ti64, SLM-Ti64, PO-TNT and SLM-TNT, respectively. All samples were sterilized by autoclaving prior to biomedical tests.

### 2.2 Surface characterization

Field emission scanning electron microscope (FESEM, JEOL JSM-6700F) was used for surface characterization. A non-contact measurement using a three-dimensional laser scanning microscope (3D LSM, VK-X260K, Keyence, Japan) was employed to evaluate the surface roughness and obtain a 3D surface topography of the specimens. At least three samples were evaluated for each configuration, and

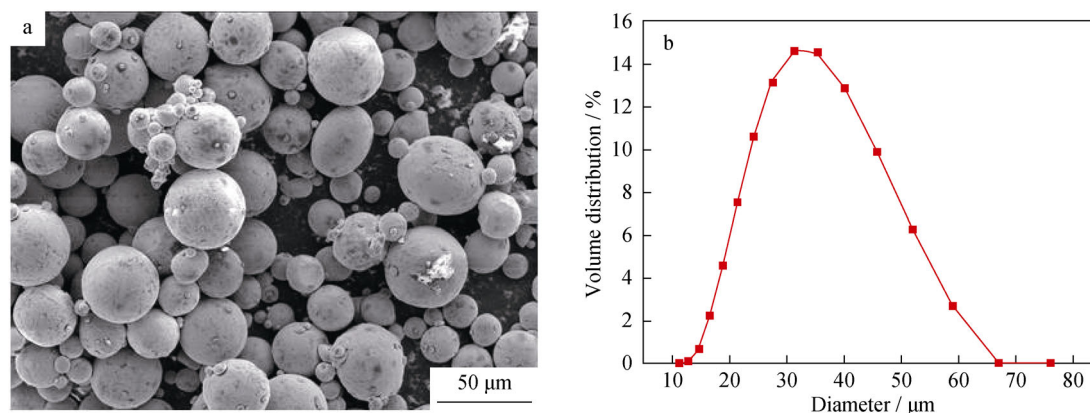


**Fig. 1** a SEM image and b size distribution of raw Ti-6Al-4V powders

three fields were acquired per group. The surface roughness parameters, i.e.,  $R_a$  (arithmetical mean deviation of the profile, ISO 4287-1997) and  $R_z$  (maximum height of the profile, ISO 4287-1997), were calculated by VK analyzer software (Keyence, Japan) according to the standard—JIS B 0601:2001 (ISO 4287:1997).

### 2.3 Initial static contact angle

The wettability studies were performed by a contact angle video system DSA 100, Krüss, Germany. An equal volume of distilled water (5  $\mu$ l) was placed at the sample surface of the samples using a microsyringe. The initial static water contact angle was immediately measured when the water droplet was deposited on the membrane surface, which better reflects the natural wettability of the material surface, and the measurements were done at least three times.

### 2.4 Protein adsorption assay

In this study, bovine serum albumin (BSA), fraction V (Sigma, purity of 99.8%) was used as the model protein, and phosphate buffer solution (PBS,  $K_2HPO_4/KH_2PO_4$ , 100  $m\cdot mol\cdot L^{-1}$ , pH 7.4) was used for the protein solution preparation. The specimens were incubated into the 1  $mg\cdot ml^{-1}$  protein solution and maintained in a sterile humidified incubator at 37 °C for 2 h. Afterward, PBS was used to remove the unbound proteins by washing the samples three times. Then each sample was removed to a new well. The proteins adsorbed on the samples were eluted after 1-h incubation at 37 °C (at least three samples were used for each configuration) by 2% sodium dodecyl sulfate (SDS) and determined by a protein assay kit (Pierce, BCA Protein Assay Kit, Rockford, Illinois, USA). The analysis was performed by using a microplate reader at 570 nm. Each protein concentration was calibrated by a standard curve with bovine serum albumin.

### 2.5 Cell isolation and culture

Rat bone mesenchymal stem cells (MSCs) were isolated from the bone shaft of the femora of 4-week-old rats and primarily cultured using the method described by Maegawa et al. [20]. The cells were obtained from at least two rats and pooled, and then seeded in a 25-cm<sup>2</sup> tissue culture flask with the Dulbecco's modified eagle medium (DMEM) containing 10% fetal bovine serum (FBS) and antibiotics (100  $U\cdot ml^{-1}$  penicillin G, 100  $mg\cdot ml^{-1}$  streptomycin sulfate and 0.25  $mg\cdot ml^{-1}$  amphotericin B) and maintained in a humidified atmosphere containing 95% air and 5% CO<sub>2</sub> at 37 °C. The medium in primary cultures was renewed every 2 days. At 80% confluence, the rat MSCs were

harvested with trypsin/EDTA, and used for following experiments.

### 2.6 Initial cell adhesion

The initial cell adhesion was evaluated by fluorescence microscope (Nikon SMZ 1000, Japan). The MSCs were seeded onto the samples pre-loaded in 24-well plates at a density of  $1 \times 10^4$  cells per sample. After incubation for 2 h, non-adhered cells were removed by rinsing with PBS. Thereafter, the attached cells on the samples were stained with calcein and observed under fluorescence microscope. Cell number was quantified from five random fields.

### 2.7 Cell morphology by SEM

After 2-h culture, the adhered cells on substrates were washed with PBS and fixed with 4% paraformaldehyde for 0.5 h. Then, the samples were washed with PBS and then dehydrated through a gradient series of ethanol (10, 30, 50, 70, 80, 90, 95, 100; vol%) for 10 min in each solution. Finally, the dried samples were gold-sputter coated for 60 s and then characterized by SEM.

### 2.8 Cell proliferation

Cell proliferation was evaluated by 3-(4, 5-dimethylthiazol-2-yl)-2, 5-diphenyltetrazoliumbromide (MTT) assay. MTT was reduced by succinate dehydrogenase in the mitochondria of live cells to insoluble blue crystals (Formazan), and the amount of formazan formed was proportional to the number of live cells [21]. MSCs were seeded on the samples with a density of  $5 \times 10^4$  cells/well in a 24-well plate. The fresh media was renewed every 2 days, and the number of cells was determined after 24, 72 and 120 h. The MTT solution (5  $mg\cdot ml^{-1}$  in PBS, 50  $\mu$ l) was added to each well containing 500  $\mu$ l culture media and incubated for 4 h at 37 °C. Then, the blue formazan reaction product was dissolved by 500  $\mu$ l dimethyl sulfoxide (DMSO) and transferred to a 96-well plate. The absorbance of each well was evaluated at 490 nm using a microplate reader.

### 2.9 Statistical analysis

SigmaStat package (Systat software GmbH, Erkrath, Germany) was used for statistics analysis. Standard analysis comparing more than two treatments was done by using the one-way ANOVA (analysis of variance). Depending on the data distribution, either a one-way ANOVA or an ANOVA on ranks was performed. Post hoc tests were Holm–Sidak or Dunn's versus the control group, respectively. Statistical values were indicated at the relevant experiments. A

statistical probability ( $p$ ) < 0.05 was considered statistically significant.

### 3 Results

#### 3.1 Surface characterization

Figure 2 shows the surface microstructures of PO-Ti64, SLM-Ti64, PO-TNT and SLM-TNT samples at both low and high magnifications. PO-Ti64 exhibits a flat polished surface without apparent features (Fig. 2a). As shown in Fig. 2b, SLM-Ti64 presents a typical SLMed surface with “ridge and valley” structures, with melt-pool boundaries lying along them. The distance between the adjacent ridge and valley is about 220  $\mu\text{m}$ , which is almost half of the hatch distance. Higher magnification micrograph confirms

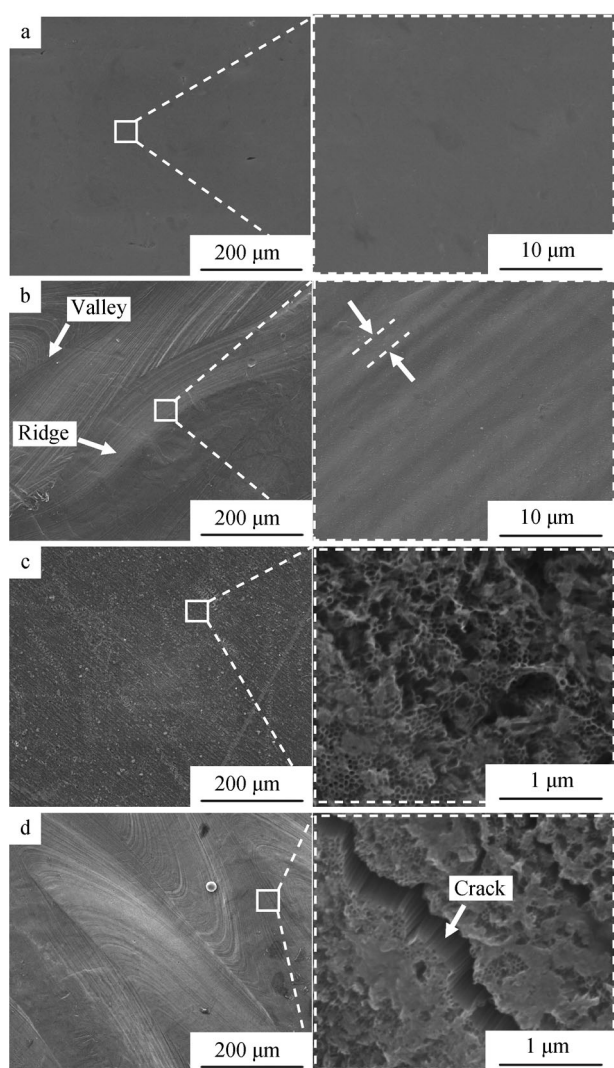


**Fig. 2** SEM images of **a** PO-Ti64, **b** SLM-Ti64, **c** PO-TNT and **d** SLM-TNT

that the distance between adjacent melt-pool boundaries is about 2–4  $\mu\text{m}$ . PO-TNT shows a flat surface at low magnification, but the high magnification image reveals that the surface of PO-TNT is composed of TNT arrays with average nanotube diameter of  $\sim 60$  nm (Fig. 2c). SLM-TNT exhibits similar surface morphology as SLM-Ti64 at macro-scale, but at nanoscale, vertically aligned TNT arrays with the same nanotube diameter ( $\sim 60$  nm) are observed (Fig. 2d). It is important to note the presence of cracks along the melt-pool boundaries on the SLM-TNT sample.

The 3D LSM was employed for topographical analyses and roughness measurements. Figure 3 shows 3D topographic images of PO-Ti64, SLM-Ti64, PO-TNT and SLM-TNT samples over an area of 710  $\mu\text{m} \times 530$   $\mu\text{m}$ , and their roughness parameters are presented in Table 1. Both PO-Ti64 and PO-TNT show smooth surface with relatively low  $R_a$ , but the latter exhibits slightly higher  $R_z$  than the former. The topographical relief of SLM-Ti64 and SLM-TNT samples seems comparable as presented in Fig. 3b, d, and there are no significant differences between the roughness parameters of these two configurations.

Figure 4 shows the initial static water contact angle measurements. Although all the samples show hydrophilic surfaces with contact angles lower than 90°, the two anodized groups exhibit significantly lower apparent contact angles (about only 10°) than the un-anodized samples.

#### 3.2 Protein adsorption, cell adhesion and proliferation

Figure 5 presents the amounts of protein adsorption on PO-Ti64, SLM-Ti64, PO-TNT and SLM-TNT samples. After incubation for 2 h, the amount of BSA adsorbed onto PO-Ti64 is only about 35–60  $\mu\text{g}\cdot\text{ml}^{-1}$  which is comparable to that onto the SLM-Ti64 but is only half of that onto PO-TNT. Generally, anodized samples absorb significantly more protein than un-anodized samples, but no significant difference is noticed between the amount of protein adsorbed on PO-TNT and SLM-TNT samples.

The numbers of MSC adhered on PO-Ti64, SLM-Ti64, PO-TNT and SLM-TNT samples after incubation for 2 h are shown in Fig. 6. Generally, the number of MSCs adhered on anodized surfaces is 1.5–2.0 times larger than those on PO-Ti64 and SLM-Ti64 samples. Although it seems that the average number of cells adhered on SLM-Ti64 is higher than that on PO-Ti64, the difference is not significant.

Figure 7 shows the morphology of MSCs cultured for 2 h on various substrates. MSC on PO-Ti64 shows a flattened morphology, and at higher magnification, evident formation of filopodia anchored to the surface is observed (Fig. 7a). The cell on SLM-Ti64 shows similar spreading level to that on PO-Ti64, but the high magnification image

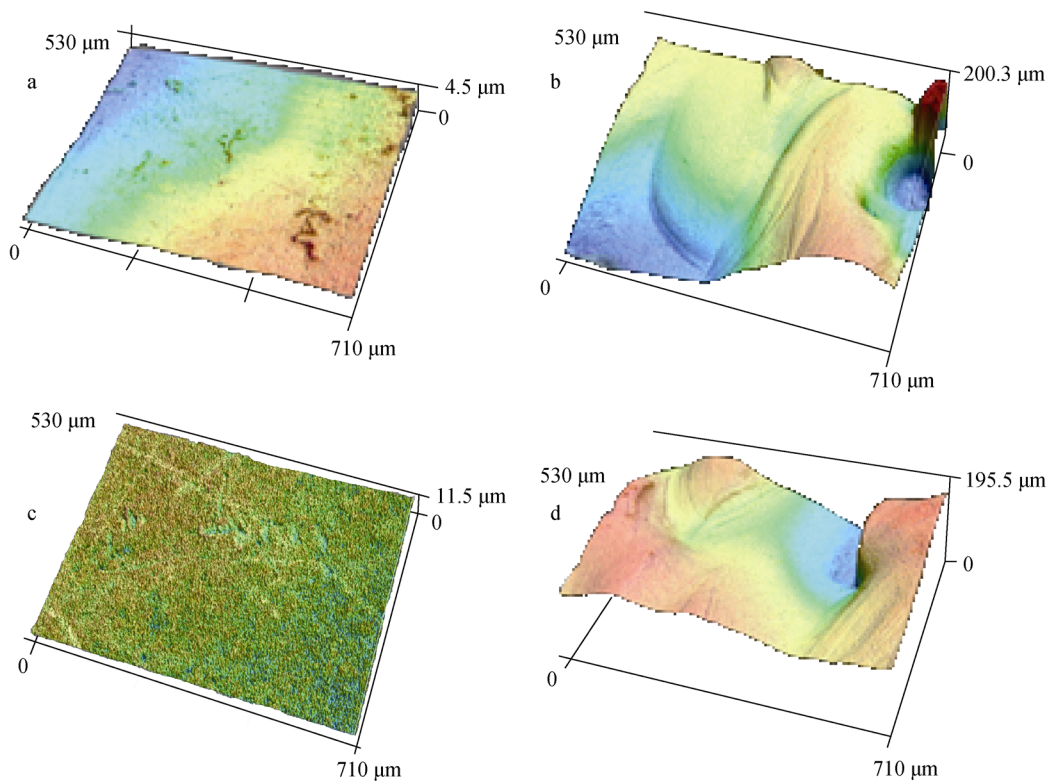


**Fig. 3** Surface topographic 3D views over an area of  $710 \mu\text{m} \times 530 \mu\text{m}$  of **a** PO-Ti64, **b** SLM-Ti64, **c** PO-TNT and **d** SLM-TNT (color scale of each profile representing height of peaks on surface)

**Table 1** Roughness parameters on studied surfaces ( $\mu\text{m}$ )

Roughness	PO-Ti64	SLM-Ti64	PO-TNT	SLM-TNT
$R_a$	0.489	0.876	0.681	0.929
$R_z$	4.5	200.3	11.5	195.5

shown in Fig. 7b reveals that MSC on SLMed surface extends more filopodia lying perpendicular to melt-pool boundaries, and the filopodia are more intimately associated with the surface in comparison with MSC on the PO-Ti64. Figure 7c, d shows that the cells adhered on PO-TNT

and SLM-TNT samples are extended with a polygonal shape attached tightly to the substrates, and the cell on SLM-TNT tends to spread perpendicular to melt-pool boundaries. In addition, nanoscale lateral membrane protrusions emanating from the cell body and the filopodia are presented at high magnification, and these nanoscale lateral membrane protrusions seem to extend along and mold the nanotube walls of both anodized groups. It should be noted that Fig. 7 only represents the spreading from a single cell for each group, not the division and proliferation of the number of cells.

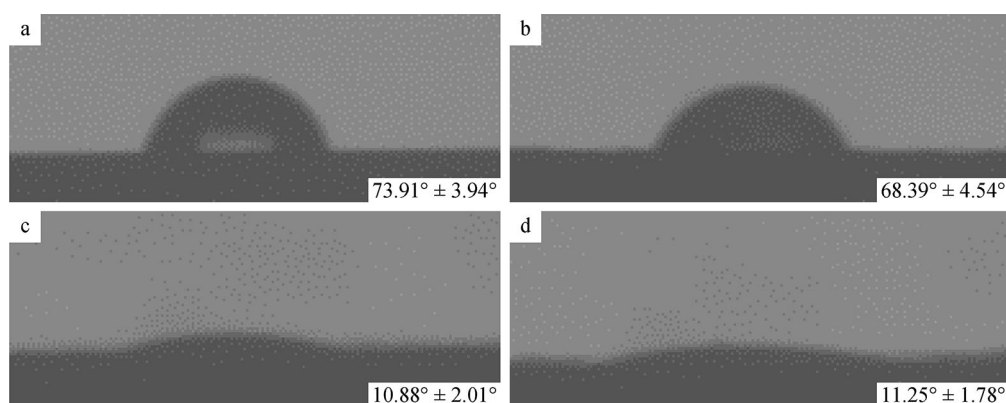


**Fig. 4** Initial static water contact angles and droplet images of **a** PO-Ti64, **b** SLM-Ti64, **c** PO-TNT and **d** SLM-TNT

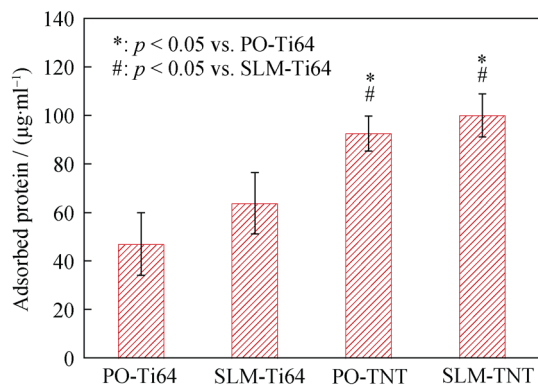


**Fig. 5** Protein absorption on samples after 2-h incubation in PBS containing 1 mg·ml<sup>-1</sup> BSA

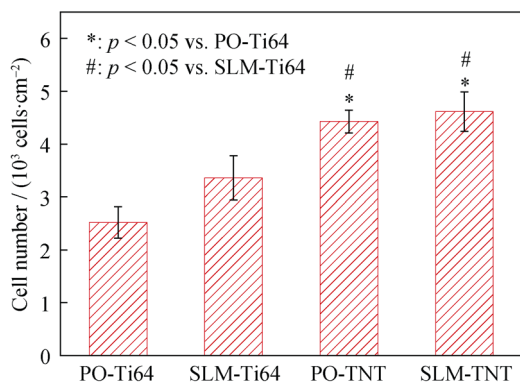


**Fig. 6** Cell counting using calcein staining after culturing for 2 h on the different substrates

Cell proliferation is assessed by MTT as presented in Fig. 8. MSCs show a time-dependent growth pattern on all the samples, i.e., a significantly higher MTT absorbance of MSCs is observed for each configuration with longer incubation time. The cell proliferation after culturing for 24 h on various substrates does not show discernible difference, but after cell culture for 72 and 120 h, the cell proliferation is significantly improved on the two anodized groups than on PO-Ti64 and SLM-Ti64 samples. In addition, the cell number on SLM-TNT is obviously larger than that on PO-TNT samples after incubation for 120 h.

**4 Discussion**

Bone is a 3D inhomogeneous tissue with unique features from macro- to nanoscales [18]. Therefore, ideally metallic implants should have similar hierarchical structures at multiple scales. In this work, a triple-scale hierarchical surface has been obtained via SLM and electrochemical anodization techniques, while polished surfaces, SLMed surfaces and polished surfaces post-anodization are also fabricated as references.

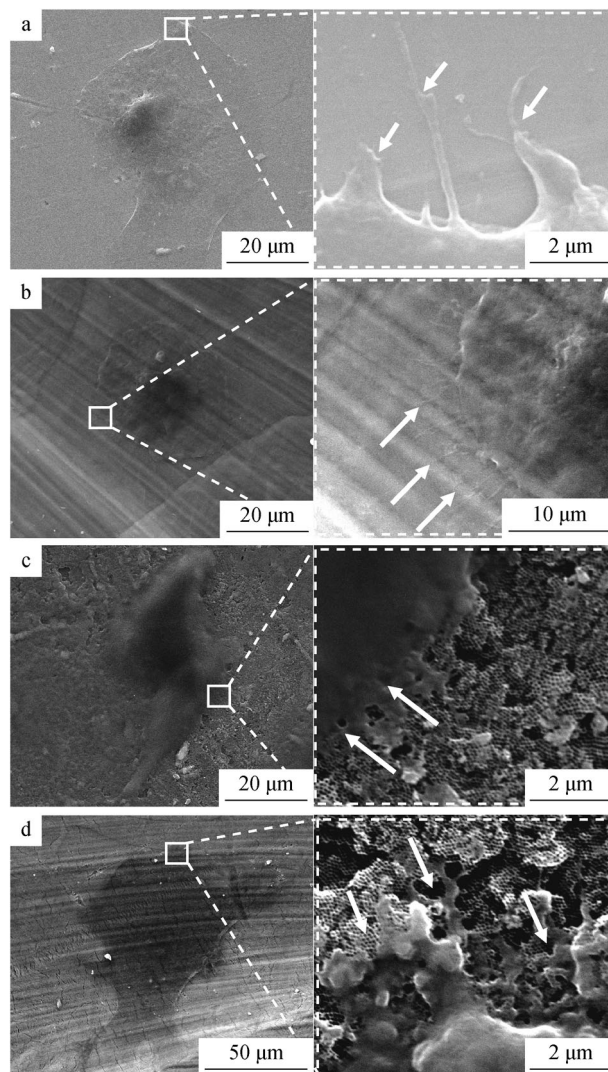


**Fig. 7** SEM images of MSCs on a PO-Ti64, b SLM-Ti64, c PO-TNT and d SLM-TNT where flopodia are indicated with arrows

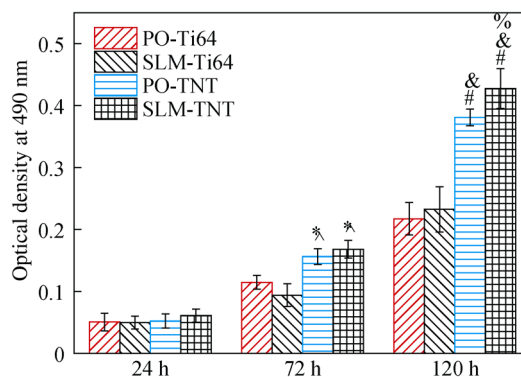


**Fig. 8** MSCs proliferation on different substrates after 24-, 72- and 120-h culture (\**p* < 0.05 vs. PO-Ti64 (72 h); ^*p* < 0.05 vs. SLM-Ti64 (72 h); #*p* < 0.05 vs. PO-Ti64 (120 h); &*p* < 0.05 vs. SLM-Ti64 (120 h); %*p* < 0.05 vs. PO-TNT (120 h))

Figure 9 shows a schematic diagram of the hierarchical structure of SLM-TNT samples. Generally speaking, the SLM-TNT samples exhibit macro-micron-nano-surface features. At the macro-scale, the “ridge and valley” structures of SLM-Ti64 and SLM-TNT samples show a topographical relief at hundreds of micron-scale (Figs. 2, 3, 9). These results are partially in agreement with the widely accepted statement that SLM is only suited for the production of the structures at the millimeter- or sub-millimeter-scale [12]. Since the average powder size is around  $35\ \mu\text{m}$  as presented in Fig. 1, it is reasonable to observe that the surface features below tens of micron-scale can hardly be obtained only via SLM. However, Fig. 2b, d shows the melt-pool boundaries with track distance of  $2\text{--}4\ \mu\text{m}$  on the two SLMed groups. Although these melt-pool boundaries exhibit length of more than hundreds of microns, they still can be viewed as micron-scale features, because in this case, the melt-pool boundaries may act as aligned textures with micron-scale spaces. Such structures would inevitably increase the specific surface area and thus affect the surface properties. At nanoscale, the formation of nanotubular structures on the surface of SLM-TNT is also influenced by these melt-pool boundaries. Compared with PO-TNT, SLM-TNT samples show cracks on the surfaces (Fig. 2d). As illustrated by Mor et al. [22], the formation of TNT array starts from the small pits on the oxide layer of Ti. The pits grow further into the substrate and are always perpendicular to the Ti surface. In this work, TNT arrays grown on the surface with high curvature may peel from the surface, because of the lack of substrate underneath these TNT arrays. Consequently, the cracks are usually found around the melt-pool boundaries. Nevertheless, the formation of these micro-cracks along melt-pool boundaries does not lead to apparent changes at macro-scale topography and roughness, as shown in Fig. 3 and Table 1, respectively.

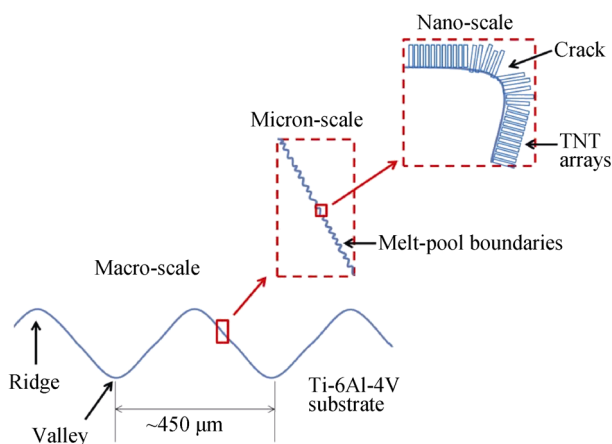


**Fig. 9** Schematic diagram of hierarchical structure of SLM-TNT sample

As stated above, SLM-TNT exhibits a triple-scale surface, so the surfaces of PO-Ti64, SLM-Ti64 and PO-TNT can be categorized as non-features, macro-micron-scale features and nanoscale features, respectively. Mohammed et al. [23] stated that a thin but dense oxide layer is always formed on the surface in a very short time when exposing Ti alloys to the air, so it is obvious that the surface chemical compositions of all samples are the same, i.e.,  $\text{TiO}_2$ . Therefore, the difference in surface topographical structures may have played a dominant role in determining the surface hydrophilicity and cytocompatibility.

The interactions between biomaterials and surrounding tissues start from the displacement of water from the interface, followed by the adsorption of a protein layer [24, 25], so the wettability and BSA adsorption have been evaluated before performing the cell assessments in this work. Figures 4 and 5 reveal that both contact angles and the protein adsorption are highly dependent on the nanoscale features, but not sensitive to the macro-micron-scale structures. However, these results are not in accordance with the generally accepted knowledge. Firstly, according to the classical theory reported by Wenzel [26], the surface roughness of a homogeneous solid surface affects the apparent contact angle ( $\theta_{\text{app}}$ ) as follows:

$$\cos\theta_{\text{app}} = R_w \cos\theta_Y \quad (1)$$

where  $R_w$  is the surface area ratio, relating to the surface roughness, and  $\theta_Y$  is the Young contact angle which is the equilibrium contact angle of ideal smooth surface. In this study, PO-Ti64 shows a flat and smooth surface without obvious features, so  $\theta_Y$  is around  $74^\circ$ , as shown in Fig. 4a. According to Eq. (1), when  $\theta_Y < 90^\circ$ , a decrease in the experimental contact angles with roughness growing can be predicted. However, SLM-Ti64 and SLM-TNT samples exhibit comparable  $R_a$  and  $R_z$ , but the apparent contact angles of the former are almost six times higher than those of the latter. Such a result should be attributed to the nanotubular structures on anodized samples. The Young's contact angle ( $\theta_Y$ ) is only determined by the surface free energy. The anodization leads to a geometric increase in the surface area ratio, thus significantly influencing the surface free energy. Consequently,  $\theta_{\text{app}}$  of SLM-TNT cannot be correctly predicted when taking  $\theta_Y$  of the un-anodized samples. Secondly, it is widely considered that hydrophobic surfaces are preferred for protein adsorption [25]. Nevertheless, the two anodized samples, exhibiting much lower contact angles, show significantly enhanced BSA adsorption in comparison with PO-Ti64 and SLM-Ti64 specimens. Such a result is also due to the nanoscale features of PO-TNT and SLM-TNT samples. On the one hand, the thin walls of TNT arrays might be preferential adsorption sites for BSA. On the other hand, TNT arrays can act as chemical carriers for drug delivery [27], so it is

reasonable to assume that higher amount of BSA is adsorbed into, instead of onto, nanotubes.

The cell responses to the various substrates are evaluated via cell adhesion and proliferation assessments (Figs. 6, 7, 8). In general, SLM-Ti64, PO-TNT and SLM-TNT exhibit enhanced or at least comparable cytocompatibility compared to the commercially available PO-Ti64, suggesting the satisfactory biocompatibility of all samples. Initial cell adhesion is a critical step that determines the ultimate fate of the cell, such as the proliferation and differentiation [28]. Considering the dominant role the protein adsorption plays in modulating cell attachment, the significantly improved cell adhesion on the anodized surfaces, showing higher amount of protein adsorption, is not unexpected. As revealed in Fig. 7, the filopodia seem to be preferential to spread perpendicular to the micron-scale melt-pool boundaries on SLM-Ti64 and SLM-TNT samples, which is in accordance with the previous investigation about the cell fate on the aligned micro-textures [29]. In addition, the lateral membrane protrusions of MSCs on PO-TNT and SLM-TNT samples demonstrate the improved cytocompatibility, resulting from the nanoscale features. It is not unexpected that the anodized groups are preferential for cell proliferation after incubation for 72 and 120 h, because TNT arrays with nanotube diameters lower than 70 nm can accelerate cell proliferation [30, 31]. It should be noted that after cell culture for 120 h, the cell proliferation on SLM-TNT is significantly higher than that on PO-TNT samples, suggesting that a macro-micron-nanoscale surface may be preferred for long-time implantation.

## 5 Conclusion

This work aims at understanding of the surface properties and cell response of the macro-micron-nanoscale SLM-TNT samples, and comparing the influence of the different scale structures on the surface roughness, hydrophilicity and cytocompatibility. The results suggest that SLM can produce a double-scale-featured surface with micron-scale melt-pool boundaries lying on the macro-scale “ridge and valley” structures. The subsequent electrochemical anodization can further fabricate TNT arrays on the surface, while cracks are formed on the places with high curvature. After comparing SLM-TNT samples with the three reference groups, it is concluded that although the nanoscale features do not lead to significant change in the surface topography and surface roughness, it should be responsible for the better wettability, enhanced protein adsorption and the improved cell adhesion and proliferation. In contrast, the macro-micron-scale structures only slightly improve the cell attachment on the materials. The better performance of the SLM-TNT compared with SLM-

Ti64 demonstrates the great potential to apply electrochemical anodization for improving the cytocompatibility of dense AMed Ti implants.

**Acknowledgements** This research was financially supported by the National Natural Science Foundation of China (No. 51604104), Shenzhen Science and Technology Innovation Commission (No. ZDSYS201703031748354) and the National Science Foundation of Guangdong Province (No. 2016A030313756).

## References

- [1] Hao YL, Li SJ, Yang R. Biomedical titanium alloys and their additive manufacturing. *Rare Met.* 2016;35(9):661.
- [2] Liu QH, Xu XJ, Ge XL, He XH, Tao J, Zhong YY. Research of laser alloying Ti-Si-C coating on TC4 titanium alloy. *Chin J Rare Met.* 2016;40(6):546.
- [3] Yu SR, Yao Q, Chu HC. Morphology and phase composition of MAO ceramic coating containing Cu on Ti6Al4V alloy. *Rare Met.* 2017;36(8):671.
- [4] Zhao D, Chang K, Ebel T, Qian M, Willumeit R, Yan M, Pyczak F. Microstructure and mechanical behavior of metal injection molded Ti-Nb binary alloys as biomedical material. *J Mech Behav Biomed Mater.* 2013;28(6):171.
- [5] Zhao D, Chang K, Ebel T, Nie H, Willumeit R, Pyczak F. Sintering behavior and mechanical properties of a metal injection molded Ti-Nb binary alloy as biomaterial. *J Alloy Compd.* 2015;640:394.
- [6] Zhao D, Chang K, Ebel T, Qian M, Willumeit R, Yan M, Pyczak F. Titanium carbide precipitation in Ti-22Nb alloy fabricated by metal injection moulding. *Powder Metall.* 2014; 57(1):2.
- [7] Wang Z, Wang C, Li C, Qin Y, Zhong L, Chen B, Li Z, Liu H, Chang F, Wang J. Analysis of factors influencing bone ingrowth into three-dimensional printed porous metal scaffolds: a review. *J Alloys Compd.* 2017;717:271.
- [8] Matena J, Petersen S, Gieseke M, Kampmann A, Teske M, Beyersbach M, Escobar H, Haferkamp H, Gellrich N-C, Nolte I. SLM produced porous titanium implant improvements for enhanced vascularization and osteoblast seeding. *Int J Mol Sci.* 2015;16(4):7478.
- [9] Li SJ, Xu QS, Wang Z, Hou WT, Hao YL, Yang R, Murr LE. Influence of cell shape on mechanical properties of Ti-6Al-4V meshes fabricated by electron beam melting method. *Acta Biomater.* 2014;10(10):4537.
- [10] Zhao S, Li SJ, Wang SG, Hou WT, Li Y, Zhang LC, Hao YL, Yang R, Misra RDK, Murr LE. Compressive and fatigue behavior of functionally graded Ti-6Al-4V meshes fabricated by electron beam melting. *Acta Mater.* 2018;150:1.
- [11] Xu W, Brandt M, Sun S, Elambasseril J, Liu Q, Latham K, Xia K, Qian M. Additive manufacturing of strong and ductile Ti-6Al-4V by selective laser melting via in situ martensite decomposition. *Acta Mater.* 2015;85:74.
- [12] Luca H, Alain R, Ralph S, Tomaso Z. Additive manufacturing of metal structures at the micrometer scale. *Adv Mater.* 2017; 29(17):1604211.
- [13] Xiao M, Chen YM, Biao MN, Zhang XD, Yang BC. Bio-functionalization of biomedical metals. *Mater Sci Eng C.* 1057;2017:70.
- [14] Amin Yavari S, van der Stok J, Chai YC, Wauthle R, Tahmasebi Birgani Z, Habibovic P, Mulier M, Schrooten J, Weinans H, Zadpoor AA. Bone regeneration performance of surface-treated porous titanium. *Biomaterials.* 2014;35(24):6172.



- [15] Xu JY, Chen XS, Zhang CY, Liu Y, Wang J, Deng FL. Improved bioactivity of selective laser melting titanium: surface modification with micro-/nano-textured hierarchical topography and bone regeneration performance evaluation. *Mater Sci Eng C*. 2016;68:229.
- [16] Nune K, Misra R, Gai X, Li S, Hao Y. Surface nanotopography-induced favorable modulation of bioactivity and osteoconductive potential of anodized 3D printed Ti-6Al-4V alloy mesh structure. *J Biomater Appl*. 2018;32(8):1032.
- [17] Beltrán-Partida E, Valdéz-Salas B, Moreno-Ulloa A, Escamilla A, Curiel MA, Rosales-Ibáñez R, Villarreal F, Bastidas DM, Bastidas JM. Improved in vitro angiogenic behavior on anodized titanium dioxide nanotubes. *J Nanobiotechnol*. 2017;15(1):10.
- [18] Wang X, Xu S, Zhou S, Xu W, Leary M, Choong P, Qian M, Brandt M, Xie YM. Topological design and additive manufacturing of porous metals for bone scaffolds and orthopaedic implants: a review. *Biomaterials*. 2016;83:127.
- [19] Wang X, Wang Y, Gou W, Lu Q, Peng J, Lu S. Role of mesenchymal stem cells in bone regeneration and fracture repair: a review. *Int Orthop*. 2013;37(12):2491.
- [20] Maegawa N, Kawamura K, Hirose M, Yajima H, Takakura Y, Ohgushi H. Enhancement of osteoblastic differentiation of mesenchymal stromal cells cultured by selective combination of bone morphogenetic protein-2 (BMP-2) and fibroblast growth factor-2 (FGF-2). *J Tissue Eng Regen Med*. 2007;1(4):306.
- [21] Cai K, Bossert J, Jandt KD. Does the nanometre scale topography of titanium influence protein adsorption and cell proliferation? *Colloids Surf B*. 2006;49(2):136.
- [22] Mor GK, Varghese OK, Paulose M, Shankar K, Grimes CA. A review on highly ordered, vertically oriented TiO<sub>2</sub> nanotube arrays: fabrication, material properties, and solar energy applications. *Sol Energy Mater Sol Cells*. 2006;90(14):2011.
- [23] Mohammed MT, Khan ZA, Siddiquee AN. Surface modifications of titanium materials for developing corrosion behavior in human body environment: a review. *Procedia Mater Sci*. 2014;6:1610.
- [24] Baier RE. Surface behaviour of biomaterials: the theta surface for biocompatibility. *J Mater Sci Mater Med*. 2006;17(11):1057.
- [25] Silva-Bermudez P, Rodil SE. An overview of protein adsorption on metal oxide coatings for biomedical implants. *Surf Coat Technol*. 2013;233:147.
- [26] Wenzel RN. Resistance of solid surfaces to wetting by water. *Ind Eng Chem*. 1936;28(8):988.
- [27] Jia Z, Xiu P, Xiong P, Zhou W, Cheng Y, Wei S, Zheng Y, Xi T, Cai H, Liu Z, Wang C, Zhang W, Li Z. Additively manufactured macroporous titanium with silver-releasing micro-/nanoporous surface for multipurpose infection control and bone repair: a proof of concept. *ACS Appl Mater Interfaces*. 2016;8(42):28495.
- [28] Zhao L, Wang H, Huo K, Zhang X, Wang W, Zhang Y, Wu Z, Chu PK. The osteogenic activity of strontium loaded titania nanotube arrays on titanium substrates. *Biomaterials*. 2013;34(1):19.
- [29] Zhao D, Lei L, Wang S, Nie H. Understanding cell homing-based tissue regeneration from the perspective of materials. *J Mater Chem B*. 2015;3(37):7319.
- [30] Oh S, Brammer KS, Li YSJ, Teng D, Engler AJ, Chien S, Jin S. Stem cell fate dictated solely by altered nanotube dimension. *Proc Natl Acad Sci*. 2009;106(7):2130.
- [31] Zhang C, Xie B, Zou Y, Zhu D, Lei L, Zhao D, Nie H. Zero-dimensional, one-dimensional, two-dimensional and three-dimensional biomaterials for cell fate regulation. *Adv Drug Deliv Rev*. 2018. <https://doi.org/10.1016/j.addr.2018.06.020>.